Supplementary Information

High-entropy alloys in radial mesostructured TiO_2 support for efficient hydrogen evolution

You Zhou[1], Yuqi Zhao[1], Jialong Li[1], Rongyao Li[1], Wendi Wang[1], Yalin He[1], Kun Lan*

[1]College of Energy Materials and Chemistry, College of Chemistry and Chemical Engineering, Inner Mongolia University, Hohhot 010021, P. R. China.

*Correspondence: k_lan@imu.edu.cn

Experimental section

Materials

Titanium butoxide ($C_{16}H_{36}O_4Ti$, 97%) and Pluronic F127 (Mw = 12,600 g mol^{-1}, $PEO_{106}PPO_{70}PEO_{106}$) were purchased from Sigma-Aldrich. Hexadecyltrimethylammonium chloride (CTAC, 97%), oleylamine (80–90%), platinum(II) acetylacetonate ($Pt(acac)_2$, 97%), copper(II) acetylacetonate ($Cu(acac)_2$, 97%), iron(III) acetylacetonate ($Fe(acac)_3$, 98%), cobalt(III) acetylacetonate ($Co(acac)_3$, 98%), nickel(II) acetylacetonate ($Ni(acac)_2$, 95%), molybdenum hexacarbonyl ($Mo(CO)_6$, 98%), and anhydrous glucose were obtained from Shanghai Aladdin Biochemical Technology Co., Ltd. Acetic acid (99.5%) was purchased from Tianjin Xinbote Chemical Co., Ltd. Hydrochloric acid (HCl, 36–38 wt.%), anhydrous ethanol (99.7%), and tetrahydrofuran (THF, 99.5%) were supplied by Sinopharm Chemical Reagent Co., Ltd. Cyclohexane (99.7%) was acquired from Macklin. Deionized water was used in all experiments. All chemicals were used as received without further purification.

Synthesis of mesoporous TiO_2 microspheres

Mesoporous TiO_2 microspheres were prepared based on our group's previous work.[1, 2] Briefly, 1.6 g of Pluronic F127 was dissolved in 30 mL of THF. Subsequently, 2.4 mL of acetic acid and 3.2 mL of concentrated HCl were added sequentially under vigorous stirring until the solution was homogeneous. Then, 3.0 mL of TBOT was introduced, forming a transparent yellow solution. This solution was then transferred into two 30 × 50 mm weighing bottles, where the solvent was evaporated at 40 °C for 22 h in a drying oven to yield a pale yellow hydrogel composed of F127/TiO_2 composite monomicelles. The hydrogel was then transferred to a 50 mL Teflon-lined autoclave and hydrothermally treated at 80 °C for 24 h. The resulting product was collected by centrifugation and washed thoroughly. Finally, the material was calcined in air at 400 °C for 3 h, with a controlled heating rate of 1 °C/min, to obtain white mesoporous TiO_2 microsphere powder.

Preparation of alloy HEA-meso-TiO_2 microspheres

CTAC (60 mg) was ultrasonically dispersed in oleylamine (30 mL) for 15 min.[3] Equimolar amounts of the metal precursors $Pt(acac)_2$, $Cu(acac)_2$, $Fe(acac)_3$, $Co(acac)_3$, and $Ni(acac)_2$, together with glucose and $Mo(CO)_6$, were then added to the dispersion, and the resulting mixture was sonicated for 45 min. Subsequently, mesoporous TiO_2 (25 mg) was introduced, followed by an additional hour of ultrasonication. The final mixture was transferred into a Teflon-lined autoclave and subjected to solvothermal treatment at 220 °C for 2 h. After cooling, the product was collected by centrifugation, washed thoroughly with ethanol and cyclohexane, and dried under vacuum to yield a brown HEA-meso-TiO_2 composite powder.

Preparation of PtCuFeCoNi HEA nanoparticles

CTAC (60 mg) was ultrasonically dispersed in oleylamine (15 mL) for 15 min.[3] Equimolar amounts of metal precursors $Pt(acac)_2$, $Cu(acac)_2$, $Fe(acac)_3$, $Co(acac)_3$, and $Ni(acac)_2$, along with glucose and $Mo(CO)_6$, were then added to the dispersion, and the mixture was sonicated for 45 min. The final mixture was transferred to a Teflon-lined autoclave and subjected to solvothermal treatment at 220 °C for 2 hours. After cooling, the product was collected by centrifugation, thoroughly washed with ethanol and cyclohexane, and dried under vacuum to yield brown PtCuFeCoNi HEA nanoparticles.

Material characterization

The morphology and microstructure of the samples were examined by field-emission scanning electron microscopy (FESEM, Hitachi S-4800) operated at an accelerating voltage of 10 kV. The nanostructures were further characterized by transmission electron microscopy (TEM), high-resolution TEM (HRTEM), and

energy-dispersive X-ray spectroscopy (EDS) elemental mapping, which were performed on an FEI Tecnai G2 F20 microscope at 200 kV. For TEM analysis, the powder sample was ultrasonically dispersed in ethanol, and a droplet of the suspension was deposited onto a carbon-coated copper grid. The crystal structure and phases were identified by X-ray diffraction (XRD) using Bruker D8 Advance with Cu Kα radiation (λ = 1.5418 Å) at 40 kV and 40 mA. Diffraction patterns were recorded in the 2θ range of 10–80° with a step size of 0.02°. Nitrogen adsorption–desorption isotherms were measured at 77 K using a Micromeritics ASAP 2020 analyzer to determine the specific surface area, pore volume, and pore size distribution. Prior to analysis, the samples were degassed under vacuum at 180 °C for 6 h. The specific surface area was calculated using the Brunauer–Emmett–Teller (BET) method, and the pore size distribution was derived from the adsorption branch of the isotherm using the Barrett–Joyner–Halenda (BJH) model. X-ray photoelectron spectroscopy (XPS) was conducted on a Thermo Scientific ESCALAB Xi+ spectrometer equipped with an Al Kα X-ray source. All binding energies were referenced to the C 1s peak at 284.8 eV. High-resolution spectra were acquired to analyze the chemical states and surface composition of relevant elements. Raman spectra were collected on a Renishaw inVia Raman microscope using 532 nm laser excitation to confirm the crystalline phase of TiO_2 and to detect possible structural modifications after HEA loading. The bulk metal composition (Pt, Cu, Fe, Co, Ni) of the catalyst was quantified by inductively coupled plasma optical emission spectrometry (ICP-OES). Before measurement, the samples were completely digested in aqua regia under heating.

Electrochemical measurements

All electrochemical measurements were performed on a Nova N402 electrochemical workstation. The hydrogen evolution reaction (HER) tests were conducted in a standard three-electrode system at room temperature, using a graphite rod as the counter electrode and a Hg/HgO electrode as the reference electrode. The working electrode was prepared by depositing catalyst ink onto carbon paper with a geometric area of 1 cm^2. The ink was prepared by ultrasonically dispersing 5 mg of catalyst powder in a mixture containing 700 μL of isopropanol, 250 μL of ultrapure water, and 50 μL of Nafion. Subsequently, 100 μL of the homogeneous ink was drop-cast onto the carbon paper surface and dried under ambient conditions to form a uniform catalyst layer. All measured potentials were converted to the reversible hydrogen electrode (RHE) scale using the following equation: E(vs. RHE) = E(vs. Hg/HgO) + 0.098 V + 0.059 × pH.

The HER performance of the catalysts was evaluated by linear sweep voltammetry (LSV) in 1.0 M KOH at room temperature. LSV curves were recorded from 0 to -0.8 V (vs. RHE) at a scan rate of 5 mV s^{-1}, with 90% iR compensation applied to correct for solution resistance. Electrochemical impedance spectroscopy (EIS) measurements were conducted at an overpotential of 100 mV (vs. RHE) over a frequency range of 100 kHz to 0.1 Hz. The resulting Nyquist plots were fitted with an appropriate equivalent circuit to extract the charge transfer resistance (Rct) and solution resistance (Rs). To estimate the electrochemically active surface area (ECSA), cyclic voltammetry (CV) was performed in the non-Faradaic potential window at scan rates of 20, 40, 60, 80, and 100 mV s^{-1}. The electrochemica double-layer capacitance (Cdl) was determined from the slope of the linear relationship between the current density difference and the scan rate. Catalytic stability was assessed via chronopotentiometry (CP) at a constant current density of 10 mA cm^{-2} for 200 hours. Tafel plots were derived from the iR-corrected LSV polarization curves. The Tafel slope was obtained by fitting the linear region to the Tafel equation: $\eta = a + b \log j$, where η is the overpotential, b is the Tafel slope, and j is the current density.

The hydrazine oxidation reaction (HzOR) and oxygen evolution reaction (OER) tests were conducted in a standard three-electrode system in 1.0 M KOH + 0.5 M N_2H_4 and 1.0 M KOH, respectively. Overall hydrazine splitting (OHzS) and overall water splitting (OWS) tests were performed in a two-electrode

system using the as-prepared catalyst as both the anode and cathode, with the electrolyte being 1.0 M KOH with or without 0.5 M N_2H_4. Linear sweep voltammetry was conducted at a scan rate of 5 mV s^{-1} to evaluate the cell voltage required to achieve different current densities. Stability was assessed by chronopotentiometry at constant current densities of 500 and 1000 mA cm^{-2}.

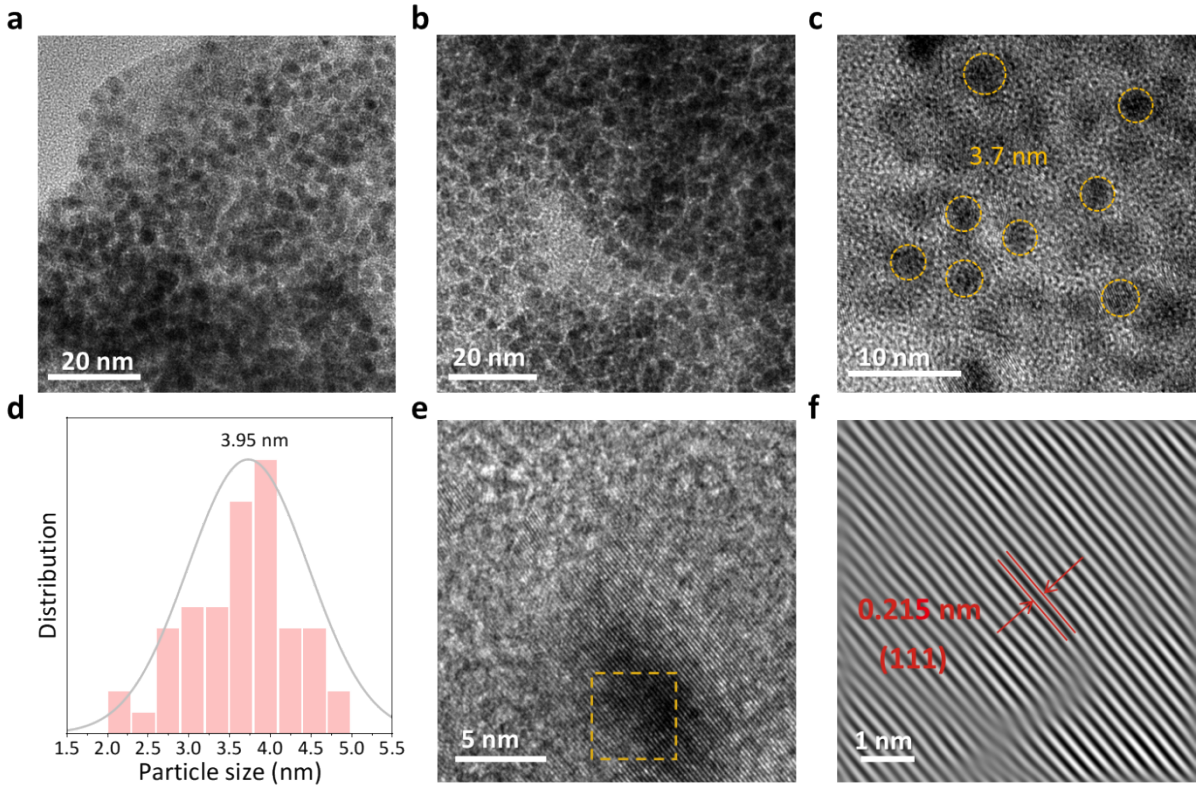

Figure S1. (a-c) TEM images of synthesized support-free HEA nanoparticles, (d) the distribution of HEA nanoparticles. (e) HRTEM image of HEA nanoparticles, and (f) the corresponding inverse fast Fourier transform (IFFT) image.

Figure S2. Photographic images for the preparation of HEA-meso-TiO_2.

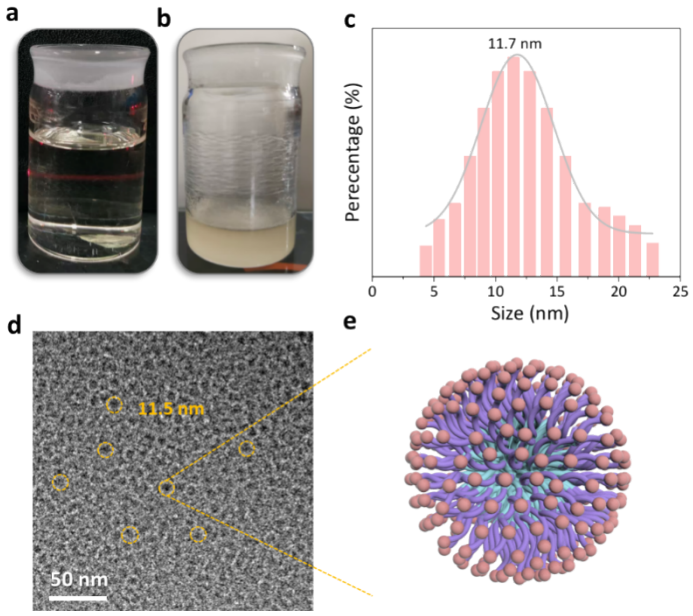

Figure S3. (a) Tyndall effect of the micelle solution, (b) photograph of the micelle gel, (c) DLS size distribution of micelles, (d, e) model and TEM image of micelles.

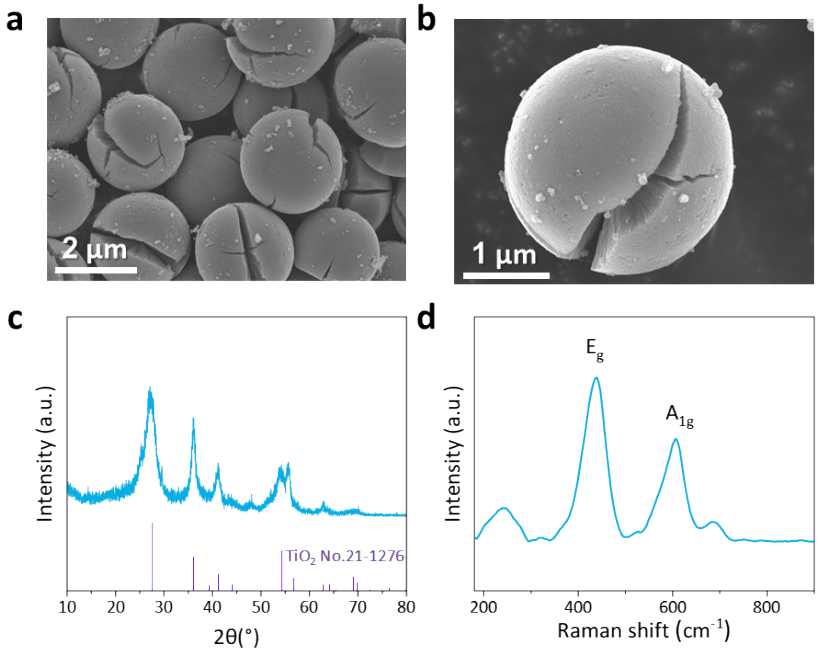

Figure S4. (a, b) SEM images, (c) XRD pattern, and (d) Raman spectrum of the uncalcined meso-TiO_2 microspheres.

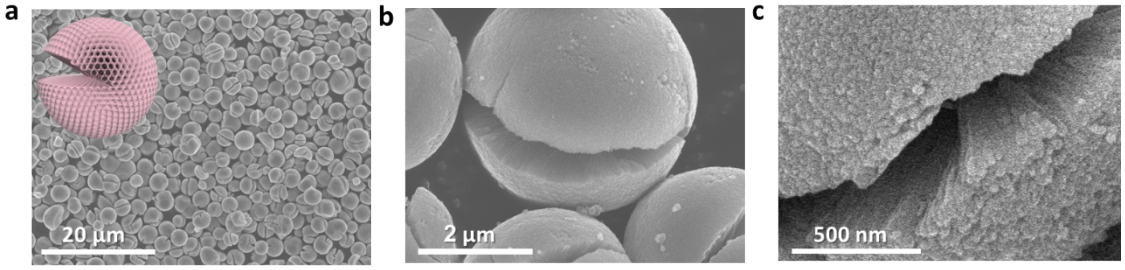

Figure S5. (a-c) SEM images of the meso-TiO_2 microspheres after calcination.

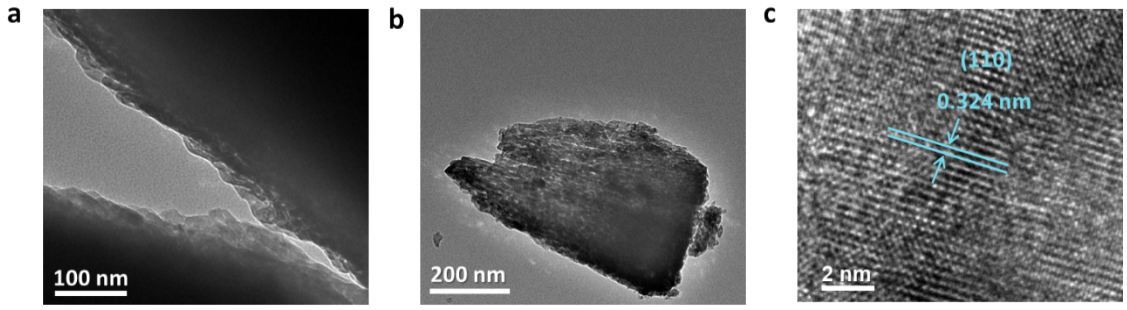

Figure S6. (a-c) TEM images of the meso-TiO_2 after calcination.

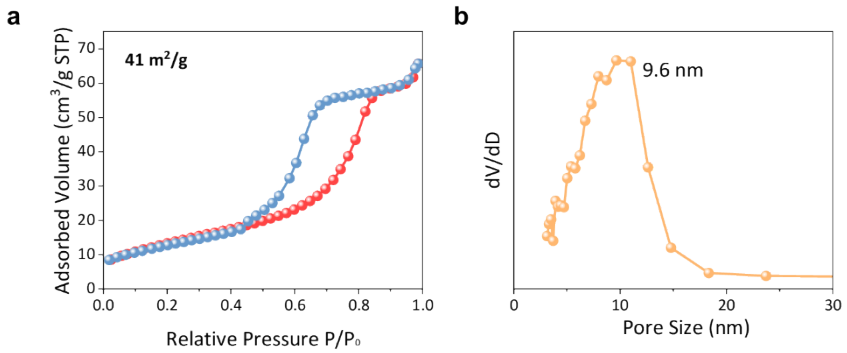

Figure S7. (a) Nitrogen adsorption–desorption isotherms and (b) Pore size distribution of the meso-TiO_2 after calcination.

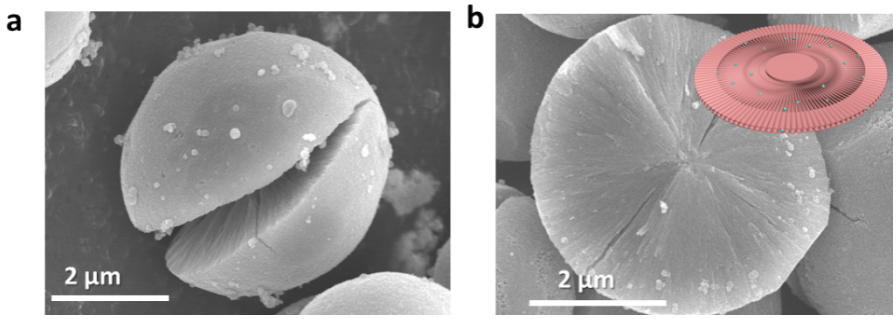

Figure S8. SEM images of (a) intact mesoporous TiO_2 microspheres and (b) fragmented mesoporous TiO_2 microspheres.

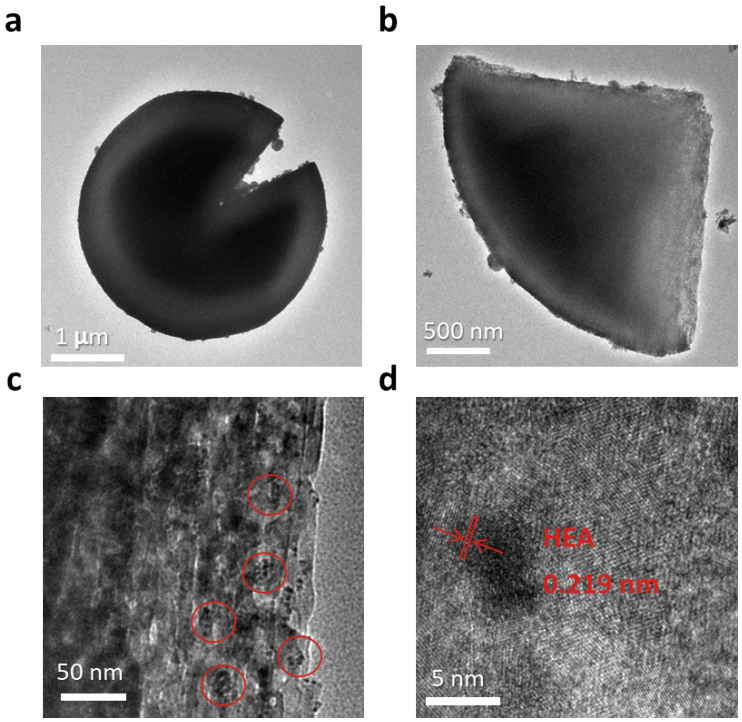

Figure S9. TEM images of (a) intact mesoporous TiO_2 microspheres, (b) fragmented mesoporous TiO_2 microspheres, (c) HEA nanoparticles confined within the mesoporous channels. (d) HRTEM image of HEA nanoparticles confined within the mesoporous channels.

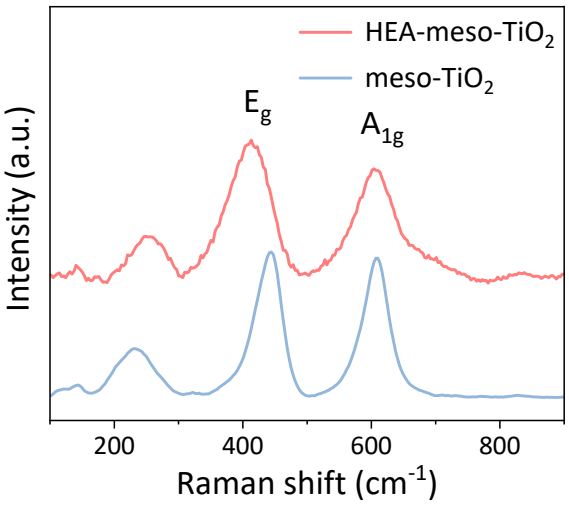

Figure S10. Raman spectra of the HEA-meso-TiO_2 and meso-TiO_2.

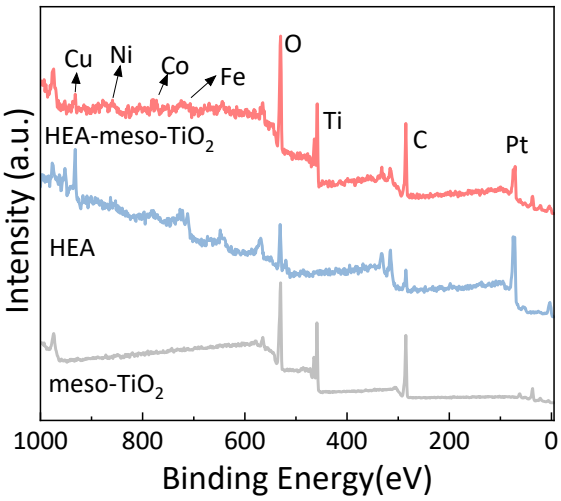

Figure S11. The XPS survey spectra of HEA-meso-TiO_2, meso-TiO_2 and HEA nanoparticles.

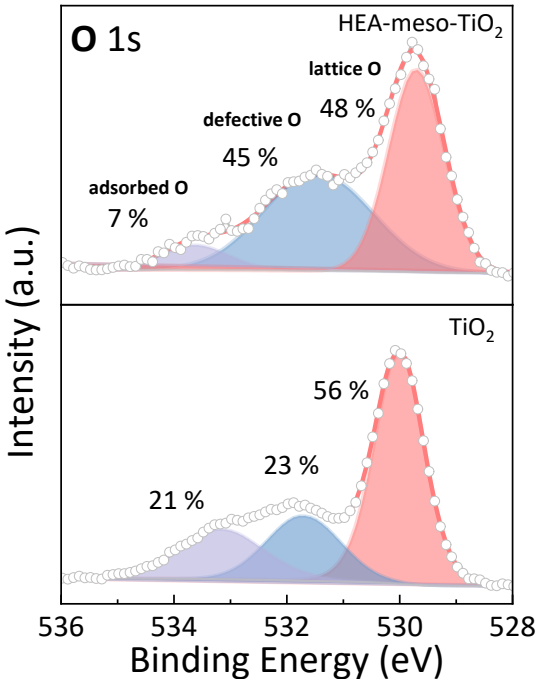

Figure S12. O 1s XPS survey spectra of HEA-meso-TiO_2 and meso-TiO_2.

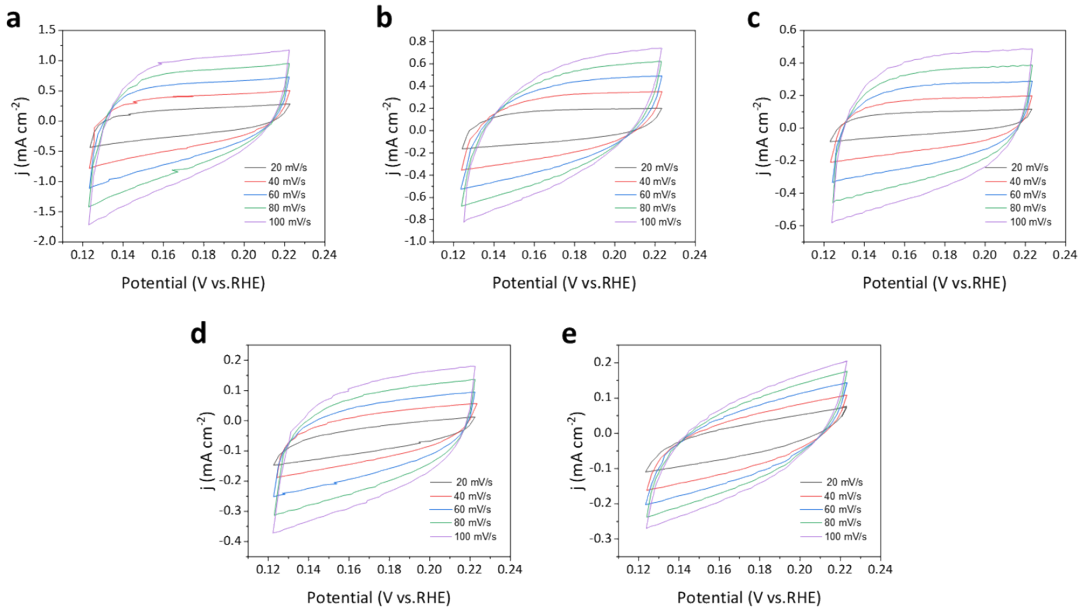

Figure S13. CV curves of different scan rates at open circuit potential for (a) HEA, (b) HEA-meso-TiO_2, (c) Pt/C, (d) meso-TiO_2, (e) P25.

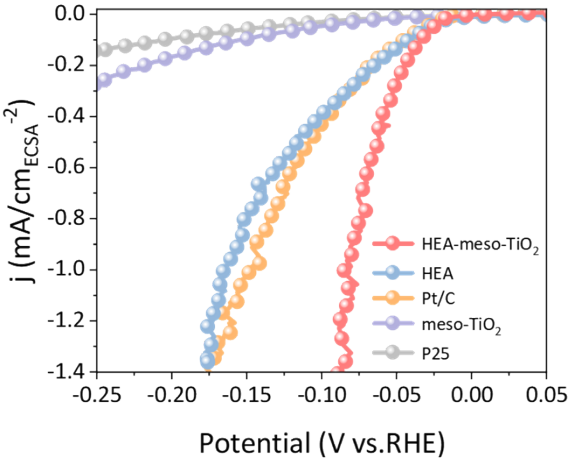

Figure S14. ECSA-Normalized LSV curves of the HEA-meso-TiO_2, HEA, Pt/C, meso-TiO_2 and P25.

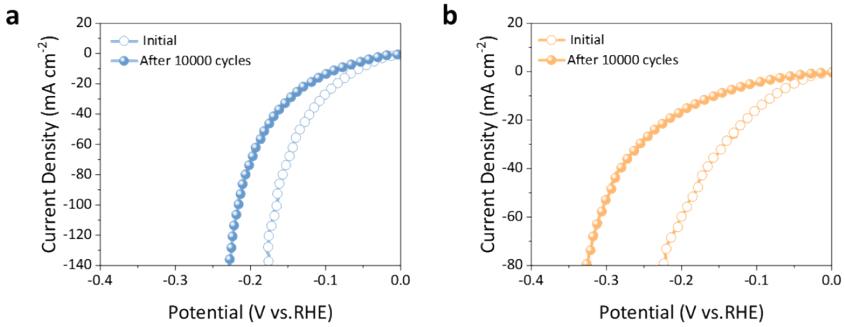

Figure S15. LSV curves of (a) the HEA-meso-TiO_2 and (b) commercial Pt/C comparison before and after 10,000 cycles.

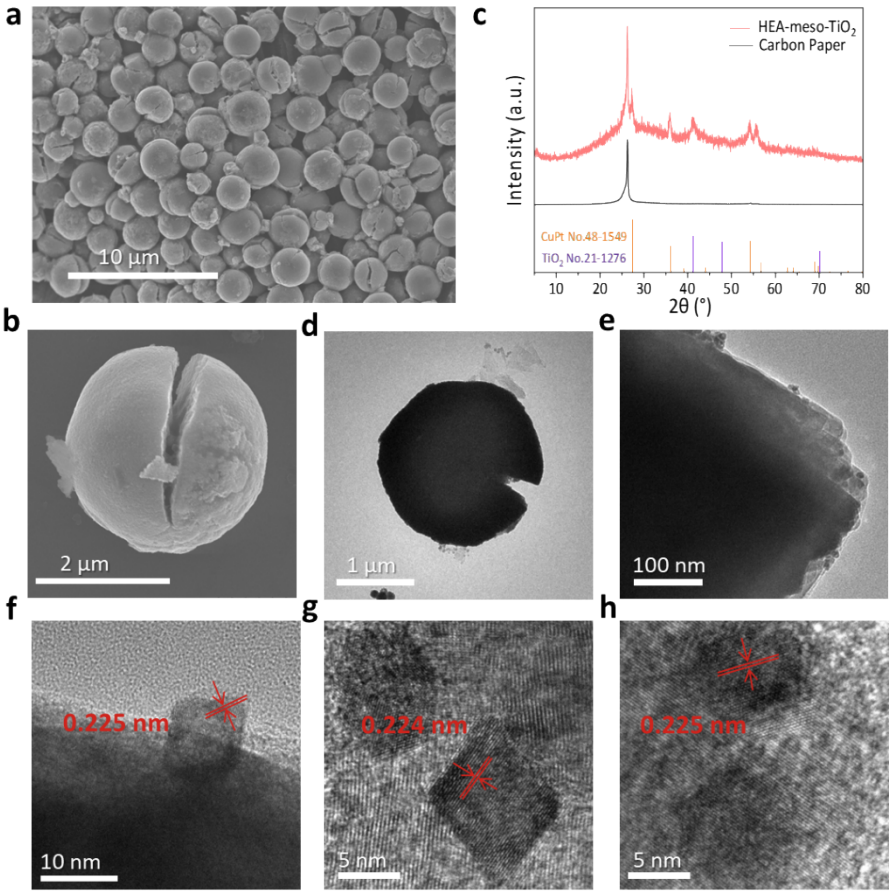

Figure S16. (a, b) SEM images, (c) XRD patterns, (d-h) TEM images after 10,000 CV cycles of the HEA-meso-TiO_2.

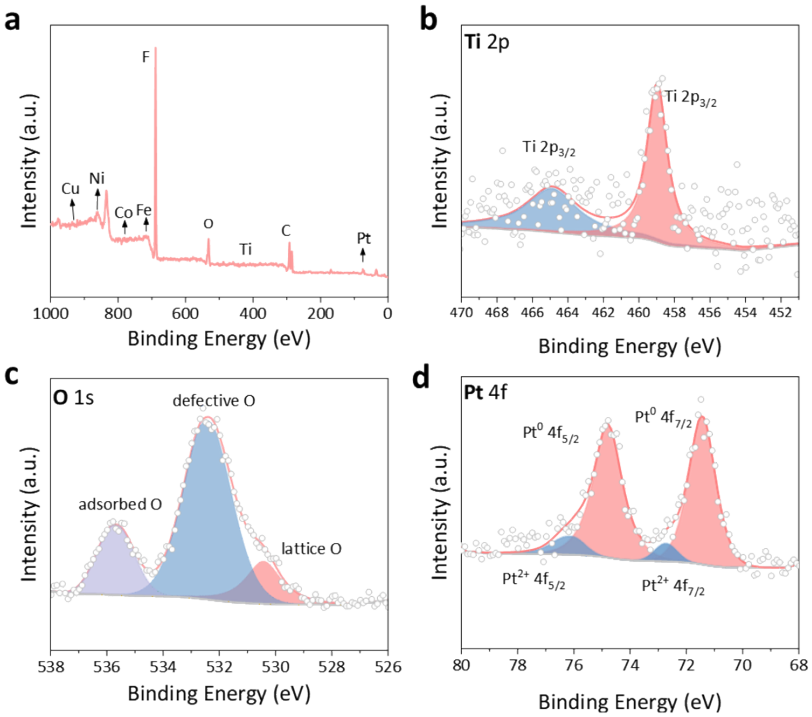

Figure S17. (a) Full-scale, (b) Ti 2p, (c) O 1s, (d) Pt 4f XPS spectra of the HEA-meso-TiO_2 after 10,000 CV cycles of HEA-meso-TiO_2.

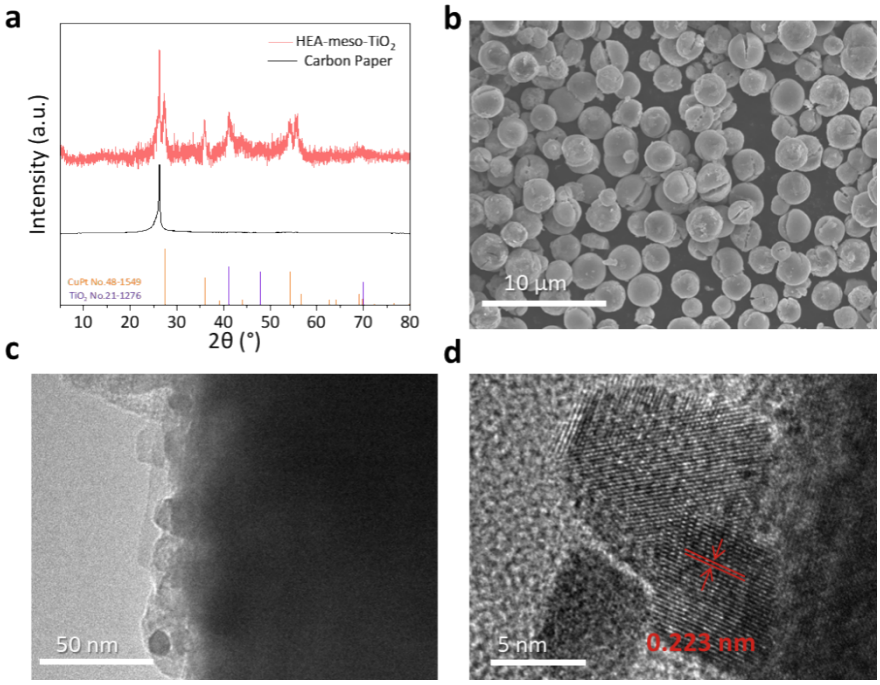

Figure S18. (a)XRD patterns, (b) SEM image, (c-d) TEM images of HEA-meso-TiO_2 after stability tests for OHzS.

Table S1. Summary of the physicochemical properties of the mesoporous TiO_2 and HEA-meso-TiO_2.

Sample	Surface area[a] ($m^2\ g^{-1}$)	Pore size (nm)	Pore volume ($cm^3\ g^{-1}$)
Meso-TiO_2	41	9.6	0.10
HEA-meso-TiO_2	15	8.1	0.05

[a] surface area calculated from the Brunauer-Emmett-Teller (BET) method by using nitrogen adsorption isotherms.

Table S2. The ICP results of the HEA-meso-TiO_2.

Element (ICP)	Atomic %	Weight %
Pt	18.1	42.2
Cu	18.3	13.9
Fe	21.2	14.1
Co	18.6	13.1
Ni	23.8	16.7

Table S3. The XPS results of the HEA-meso-TiO_2.

Element (XPS)	Atomic %	Weight %
Pt	15.4	37.6
Cu	14.6	11.7
Fe	26.7	18.8
Co	17.1	12.6
Ni	26.2	19.3

Table. S4 XPS peak area ratios of HEA and HEA-meso-TiO_2.

Sample	Element	Species	Main Peak BE (eV)	Area (CPS.eV)	Area Ratio (%)
HEA	Pt	Pt^0	71.46	5912	**66**
		Pt^{2+}	72.23	3031	**34**
	Cu	Cu^0	932.13	5630	**61**
		Cu^{2+}	933.98	3588	**39**
	Fe	Fe^0	711.49	5914	**65**
		Fe^{2+}	713.93	3324	**35**
	Co	Co^0	778.26	1906	**58**
		Co^{2+}	785.63	1356	**42**
	Ni	Ni^0	852.98	3016	**55**
		Ni^{2+}	855.66	2434	**45**
HEA-meso-TiO_2	Pt	Pt^0	71.02	2153	**61**
		Pt^{2+}	71.86	1350	**39**
	Cu	Cu^0	931.75	1445	**57**
		Cu^{2+}	932.88	1110	**43**
	Fe	Fe^0	710.78	2097	**42**
		Fe^{2+}	714.64	2880	**58**
	Co	Co^0	777.75	1294	**44**
		Co^{2+}	784.95	1682	**56**
	Ni	Ni^0	852.23	1489	**45**
		Ni^{2+}	855.68	1844	**55**

Table. S5 The Rct of HEA-meso-TiO_2 and other comparison samples fitted by Zview.

Sample	Rs (Ω)	Rct (Ω)
HEA-meso-TiO_2	1.08	3.70
HEA	1.60	4.51
Pt/C	1.75	4.68
meso-TiO_2	1.65	10.68
P25	1.39	14.60

Table S6. A survey of electrocatalytic performances of the recently reported catalysts in HER.

Catalysts	Electrolyte	Overpotential $_{(10\ mA\ cm-2)}$ (mV)	Tafel slope (mV dec^{-1})	References
HEA-meso-TiO_2	1.0 M KOH	31	24	This work
PtFeCoNiCuCr@HCS	1.0 M KOH	29	39.24	[4]
CuNiMoWCo@CF	1.0 M KOH	85.2	86.3	[5]
PdFeCoNiCu/C	1.0 M KOH	18	39	[6]
PdPtCuNiP	1.0 M KOH	32	37.4	[7]
FeCoPdIrPt@GO	1.0 M KOH	42	82	[8]
FeCoNiMnRu	1.0 M KOH	32	44	[9]
CrFeCoNiRu-RuNi	1.0 M KOH	48	48.5	[10]
Pt/TiO_2@TiC/Pt	1.0 M KOH	58	66.17	[11]
Pt@R/A-TiO_2	1.0 M KOH	49.6	49.77	[12]

References

1. K. Lan, R. Wang, W. Zhang, Z. Zhao, A. Elzatahry, X. Zhang, Y. Liu, D. Al-Dhayan, Y. Xia and D. Zhao, Chem, 2018, **4**, 2436–2450.
2. K. Lan, R. Wang, Q. Wei, Y. Wang, A. Hong, P. Feng and D. Zhao, Angew. Chem. Int. Ed., 2020, **59**, 17676–17683.
3. H. Li, Y. Han, H. Zhao, W. Qi, D. Zhang, Y. Yu, W. Cai, S. Li, J. Lai, B. Huang and L. Wang, Nat. Commun., 2020, **11**, 5437.
4. Y. Wan, W. Wei, S. Ding, L. Wu, H. Qin and X. Yuan, Adv. Funct. Mater., 2024, **35**, 2414554.
5. S. Liu, Y. Wang, T. Jiang, S. Jin, M. Sajid, Z. Zhang, J. Xu, Y. Fan, X. Wang, J. Chen, Z. Liu, X. Zheng, K. Zhang, Q. Nian, Z. Zhu, Q. Peng, T. Ahmad, K. Li and W. Chen, ACS Nano, 2024, **18**, 4229–4240.
6. D. Zhang, Y. Shi, H. Zhao, W. Qi, X. Chen, T. Zhan, S. Li, B. Yang, M. Sun, J. Lai, B. Huang and L. Wang, J. Mater. Chem. A, 2021, **9**, 889–893.
7. S. Gao, S. Hao, Z. Huang, Y. Yuan, S. Han, L. Lei, X. Zhang, R. Shahbazian-Yassar and J. Lu, Nat. Commun., 2020, **11**, 2016.
8. Z. Jia, K. Nomoto, Q. Wang, C. Kong, L. Sun, L. C. Zhang, S. X. Liang, J. Lu and J. J. Kruzic, Adv. Funct. Mater., 2021, **31**, 2101586.
9. G. Liu, C. Song, X. Li, Q. Jia, P. Wu, Z. Lou, Y. Ma, X. Cui, X. Zhou and L. Jiang, Chem. Eng. J., 2025, **509**, 161070.
10. Y. Feng, Q. Ma, W. Zhu, K. Harrath, Y. Wei, Y. Wang, Y. Qi, J. Zhang, W. Li, J. Zhu, Y. Lei, J. Huang, B. Wu and W. Zhao, Small, 2025, **22**, e10098.
11. C. E. Park, G. H. Jeong, J. Theerthagiri, H. Lee and M. Y. Choi, ACS Nano, 2023, **17**, 7539–7549.
12. W. Wu, K. Zhang, S. Wei, Y. Wang, Z. Zhang, P. Guo and G. Liu, Chem. Eng. J., 2024, **496**, 154030